Experimental investigation on the fatigue and fracture toughness properties of hypereutectoid rail steel

Schotsman, B.; Mattos Ferreira, V.; Leonetti, D.; Petrov, R. H.; Santofimia, M. J.; Sietsma, J.

DOI
10.1016/j.engfracmech.2024.110657

Publication date
2025

Document Version
Final published version

Published in
Engineering Fracture Mechanics

Engineering Fracture Mechanics 313 (2025) 110657

Contents lists available at ScienceDirect

Engineering Fracture Mechanics

journal homepage: www.elsevier.com/locate/engfracmech

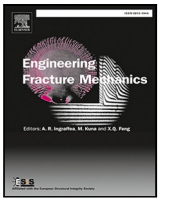

Experimental investigation on the fatigue and fracture toughness properties of hypereutectoid rail steel

B. Schotsman [a,b,*], V. Mattos Ferreira [a], D. Leonetti [c], R.H. Petrov [a,d], M.J. Santofimia [a], J. Sietsma [a]

[a] Delft University of Technology, Department Materials Science and Engineering, Mekelweg 2, 2628 CD, Delft, The Netherlands
[b] ProRail, Moreelsepark 3, 3511 EP, Utrecht, The Netherlands
[c] Eindhoven University of Technology, Eindhoven, The Netherlands
[d] Ghent University, Department of Electrochemical, Systems and Metal Engineering, Technologiepark 46, Ghent, Belgium

ARTICLE INFO

Keywords:
Hypereutectoid
Crack growth
Fracture toughness
LEFM
Fractography

ABSTRACT

Increasing train speeds and the reduction of maintenance slots places high demands on the railway rails. To meet the challenging demands, producers regularly introduce new steel types. In this experimental investigation is the mechanical behavior of an air-cooled vanadium-alloyed hypereutectoid rail steel presented. The rail is produced applying conventional hot rolling of a reheated bloom and is then cooled on a cooling bed. The mechanical behavior is determined by performing standardized linear elastic fracture mechanics tests. The necessary specimens are extracted from new rails that are made in series production. Monotonic tensile test results have shown that the strain-hardenability of the steel is comparable to standard grade eutectoid rail steel and is higher than that of an accelerated-cooled eutectoid rail grade. The fracture toughness test results showed, statistically, no difference when compared with the fracture toughness values of the accelerated-cooled eutectoid rail grade. The tests were performed at room temperature. The fatigue crack growth rates are, in the linear Paris-regime, slightly higher than in the previously mentioned steels. The results are explained considering the distinct microstructural characteristics of the air-cooled vanadium-alloyed hypereutectoid steel and the fractured surface of the specimens. This experimental investigation contributes to selecting railway steels and predicting the actual in-service behavior.

1. Introduction

The increasing train speeds and wheel loads in modern railway operations impose additional requirements on the railway track substructure, and more specifically on the rails. Moreover, the increasingly busy traffic limits the inspection and maintenance options, in both duration and frequency. Therefore infrastructure managers have introduced a damage-tolerant maintenance methodology. In addition, a reduction in rail wear is preferred since material consumption, like steel rails, is the major contributor to the carbon emissions of the railroad [1]. To enable further progress of railways, development of the rail steels is required.

As rails are hot rolled from continuously casted blooms, rail producers can choose to improve the strength and wear resistance by changing the steel composition or by introducing a post-rolling heat treatment, depending on the rolling mill facilities.

The design of the post-rolling heat treatment of rails is generally simple and consist of accelerated cooling to approximately 500 °C followed by air-cooling. Accelerated cooling limits carbon diffusion between cementite and ferrite in the typically pearlitic

* Corresponding author at: Delft University of Technology, Department Materials Science and Engineering, Mekelweg 2, 2628 CD, Delft, The Netherlands.
E-mail address: b.schotsman@tudelft.nl (B. Schotsman).

https://doi.org/10.1016/j.engfracmech.2024.110657
Received 8 September 2024; Received in revised form 4 November 2024; Accepted 12 November 2024
Available online 20 November 2024

Nomenclature

α	Geometric factor
σ	Stress (MPa)
σ_{UTS}	Ultimate tensile stress (MPa)
σ_y	0.2%-offset yield strength (MPa)
ε	Strain
a	Crack length (m)
$\mathrm{d}a/\mathrm{d}n$	Crack growth rate (m/cycle)
B	Specimen thickness (m)
C	Paris–Erdogan material parameter (m/cycle/(MPa $\sqrt{\mathrm{m}})^m$)
$C(T)$	Compact tension
E	Young's modulus of elasticity (GPa)
HV	Vickers hardness (HV)
I	Plane-strain condition
K	Stress-intensity factor (MPa $\sqrt{\mathrm{m}}$)
K_Q	Provisional K fracture toughness (MPa $\sqrt{\mathrm{m}}$)
ΔK	Stress-intensity factor range (MPa $\sqrt{\mathrm{m}}$)
m	Paris–Erdogan material parameter
n	Strain hardening exponent
P	Applied load (N)
P_Q	Intersection of the offset line and the load displacement record (N)
R	Load ratio
S_Q	Secant offset
T	Temperature (°Celsius)
u	Crack mouth opening compliance (mm)
v	Clip gauge opening displacement (mm)
W	Specimen width (m)

steels, resulting in a smaller lamellar thickness and an increase of the yield strength. Between lamellar thickness and yield strength a Hall–Petch relationship is obeyed [2–4].

In terms of steel composition, traditionally, the carbon content has been increased to improve wear resistance and strength. However, this practice introduces the risk of undesired grain boundary embrittlement because of the formation of a cementite network on the prior austenite grain boundaries. In hyper-eutectoid steels, silicon is often added to suppress cementite formation at prior austenite grain boundaries. Furthermore, vanadium is added to increase the wear resistance [5,6]. Wilby et al. [6], as an example, reported better wear properties for the air-cooled vanadium-alloyed steel compared to the accelerated-cooled pearlitic steel, having approximately the same hardness. Additionally, vanadium-carbide formation consumes carbon, effectively reducing the local carbon content. However this is not sufficient to prevent coarse cementite particles from precipitating in the thin pro-eutectic ferrite layer [7].

Minimum values for fracture toughness of rail steel are common requirements for quality control and material acceptance. High fracture toughness promotes easier inspectability of the rails due to the larger allowable crack size. To explain the microstructure characteristic and fracture toughness relationship in pearlitic steels studies focus on the prior-austenite grain size and lamellar thickness.

The size of prior-austenite grains (PAGs), in which the pearlite colonies have nucleated, is found to control the fracture toughness [8–10]. Crack path analysis showed that the cleavage fracture propagates through the (100) crystallographic plane of the ferrite following low-angle grain boundaries between pearlite colonies, i.e. between colonies with a comparable crystallographic orientation. An analysis of the angles between colonies in large and small PAGs steels further showed that large PAGs are associated with the majority of colony misorientations being below 5°, whereas in small-PAGs steels misorientations are uniformly distributed over the classes below 5°, below 10°, and over 10° misorientation [10]. These PAGs related size of 'orientation units', consisting of adjacent pearlite colonies of common parentage and therefore common orientation, control the fracture toughness [10].

Other researchers point at lamellar thickness as the microstructure property explaining the fracture toughness [4,11,12]. The highest fracture toughness values were found for steels with the highest lamellar thickness. Kavishe and Baker [4] explained the result by the actual size of the fracture process zone, which is small compared to the yielding area at the crack tip, and always smaller than the prior-austenite grain.

Fatigue crack growth has also been studied with respect to the pearlite microstructure characteristics and the fracture mechanism, but with inconclusive results [13]. Gray et al. [14] and Daeubler et al. [15] independently performed crack growth tests on American

ISO1080 eutectic railway steel. Using C(T)-specimens, it was concluded by Gray et al. that coarsening the prior austenite grain structure reduces the fatigue crack growth rate [14]. Using a tensile-tensile test setup and a stress ratio $0 < R < 1$, Daeubler et al. concluded the opposite; fine PAG size and small lamellar thickness result in the lowest crack propagation rate [15]. A complicating factor explaining crack growth is that both the orientation of the crack as well as the mechanism of crack growth change with the increase of stress-intensity factor range, ΔK, consequently affecting the crack path at the mesoscale. At low ΔK, the crack propagates in the ferrite between the cementite lamellae [13,14]. The cementite lamellae act as a boundary for local yielding and a smaller lamellar distance retards the crack propagation [13–15]. In the stable crack-propagation stage, the Paris regime, the crack propagation is stress-controlled, causing a staircase morphology at the fractured surface, of which the size is related to the lamellar thickness. At a further increase of ΔK, such that the maximum stress intensity approaches its critical value, and the crack growth is close to being unstable, the staircase features are replaced by cleavage planes and the surface gradually becomes similar to a cleavage fracture surfaces [13,16].

In the present study, the fatigue crack growth rate and fracture toughness of an air-cooled hypereutectoid rail steel are evaluated using linear elastic fracture mechanics tests. The testing procedure for the determination of fatigue crack growth rate in steels is regulated by relevant international standards, such as the ASTM E647 [17]. The testing procedure in the ASTM E399 standard [18] has been developed and standardized to measure plane-strain fracture toughness of metallic materials under Mode-I loading. The objective of this procedure is to determine the size-independent material property K_{IC}, defined in terms of the stress intensity factor, K [19]. In practice, the material is tested on specimens containing a crack that nucleates from a starter notch due to fatigue. The plane-strain fracture toughness under other modes of opening has been correlated to K_{IC} [20]. One of the challenges of railway operations is the control of rolling contact fatigue in the rails. Due to the occurrence of cyclic loading, cracks initiate and propagate at an angle of 20° - 30° with respect to the rolling surface [21]. At these initial stages, the fatigue crack growth is driven by mixed-mode conditions. At a later stage of crack propagation, it has been observed that rolling contact fatigue cracks, outside the volume affected by the presence of the rail-wheel contact stresses, tend to grow downwards, i.e. in the vertical plane [21,22]. For these reasons, fracture toughness and fatigue crack growth rate under mode-I loading will, besides serving as a benchmark, also provide insight on the microstructural behavior of rail steel.

The objective of the experimental study is therefore to determine the mechanical behavior of the air-cooled hypereutectoid rail steel using linear elastic fracture mechanics (LEFM) tests. A fractographic analysis of the fatigue crack growth, fracture toughness and tensile specimens, is made to study the crack path and relation with the microstructure characteristics of this steel, in line with a previous study by Mattos Ferreira [7]. The results are further benchmarked with results on accelerated-cooled eutectoid rail steel, using the same test setup [23,24], and eutectoid rail steels [9,25] from the literature.

2. Materials and methods

2.1. Materials

Table 1 shows the chemical composition of the air-cooled hypereutectoid rail steel, R335V, together with the accelerated-cooled eutectoid rail steel, R350HT, and the eutectoid rail steels, Ref1 and Ref2. Specific for R335V is the 0.10 wt% vanadium and ~0.9 wt% silicon addition. The composition is within the composition ranges as provided by the prEN13674-1-standard [26].

The microstructure is further defined by the production route. The R335V rail is hot rolled from a reheated bloom and subjected to air-cooling. The typical temperature at the last rolling step is $T \approx 1050\,°C$. The cooling rate during transportation to the cooling bed is ~1 °C/s and the temperature when arriving there is ~800 °C. The typical cooling rate on a cooling bed is ~0.1 °C/s [27].

The composition of R350HT accounts for a lower carbon and silicon content, and a higher manganese content when compared with R335V steel. During production, R350HT steel rail is hot rolled followed by accelerated cooling to ~500 °C and is then air-cooled, resulting in a smaller lamellar thickness.

The chemical composition of both eutectoid rail steel grades, Ref1 [9] and Ref2 [25], are included in the bottom section of Table 1.

Table 1
Chemical composition (in wt.%) of air-cooled hypereutectoid steel, R335V, the referenced accelerated-cooled eutectoid rail steel, R350HT, and eutectoid rail steels, Ref1 and Ref2.

Steel	Element concentration (wt.%)				Steel type
	C	Mn	Si	V	
R335V [7,24]	0.91	0.88	0.87	0.10	HP335
R335V [23]	0.91	0.86	0.88	0.10	HP335
R350HT [23]	0.77	1.10	0.39	–	R350HT
Ref1 [9]	0.74	1.06	0.27	–	R260
Ref2 [25]	0.68	1.11	0.35	–	900A

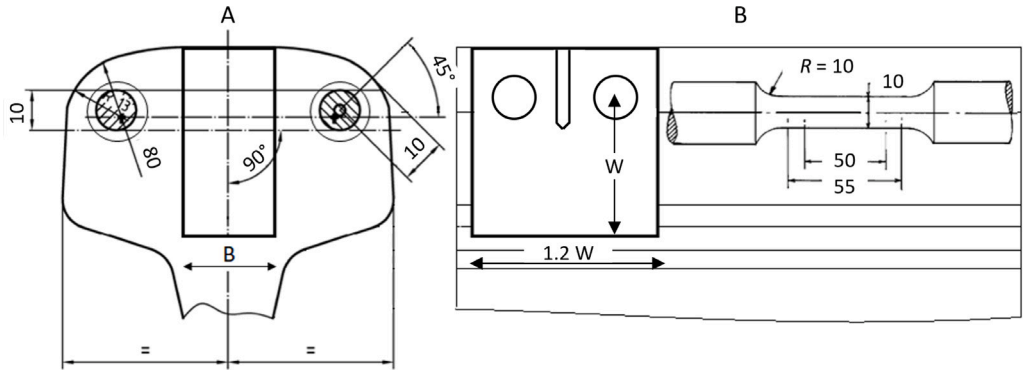

Fig. 1. Location, orientation, and dimensions [mm] of C(T)- and tensile-specimens in the rail profile. (A) The rail head cross-section. (B) The longitudinal section.

Table 2
Linear elastic fracture mechanics tests on R335V rail steel; references, specimen type, dimensions, and number of tests.

Test	Reference	Specimen type	Dimensions (mm)	Number
Fatigue crack growth	ASTM E647 [17]	C(T)	$W = 40$, $B = 10$	4
Fracture toughness	ASTM E399 [18]	C(T)	$W = 40$, $B = 18$[a]	4
			$W = 40$, $B = 20$[b]	3

[a] Specimens extracted from a UIC56-rail profile [26]; the rail head dimensions limits the thickness to $B = 18$ mm; specimens 1–4.
[b] Specimens extracted from a UIC60-rail profile [26]; specimens 5–7.

2.2. Fracture mechanics tests

2.2.1. Tensile tests

Fig. 1 presents the position of the cylindrical tensile specimens extracted from the rail head. This position is in accordance with the prEN13674-1-standard [26]. The tensile test specimens are produced, using a turning process, from a strip which has been cut from both sides of the rail profile. The test specimen position is in the center of the strip.

The monotonic tensile tests were performed using an Instron 5985 universal testing system equipped with a self-aligning wedge grip fixture and a 250 kN load cell. The elongation was measured with an Instron AVE 2 non-contacting video extensometer. A constant crosshead separation speed of 0.75 mm/min is chosen which corresponds to a strain rate $\dot{\epsilon_L} = 0.25 \times 10^{-3}\,\mathrm{s}^{-1}$ according to the EN-ISO6892-1-standard [28]. The specimens were maintained at 200 °C for 6 h before performing the tests, to relax near-surface stresses due to specimen production as prescribed in the EN13674-1-standard [26].

2.2.2. Fatigue crack growth and fracture toughness tests

Table 2 presents the relevant information on the C(T)-specimens used to quantify the fatigue crack growth rate and plane-strain fracture toughness. Fig. 1 presents the specimen position in the rail head section, which is the center of the rail head with the straight notch pointing downwards, aligning with the crack propagation orientation in in-service rail [21,22]. The C(T)-specimens are produced by face milling. The holes are drilled and reamed on the same machine before polishing the surfaces. The straight notch is cut using electric discharge milling.

The test performance and analysis follow the ASTM-E647 [17] and ASTM-E399-standards [18]. Specifically for fracture toughness determination the requirements for static testing are followed. Both fatigue crack growth and plane-strain fracture toughness tests have been performed in a testing frame equipped with a hydraulic actuator and a load cell with a nominal capacity of 125 kN, using closed-loop control and force feedback. The data acquisition system from National Instruments has a sampling frequency of 300 Hz. The specimens were loaded through a clevis and pin, designed according to the aforementioned standards. Both clevises are connected to the load line using spherical hinges to minimize secondary bending moments. The loading frequency is 10 Hz and has a sinusoid waveform. At the selected frequency self-heating is limited [29,30], has a negligible influence on the results, and is not further included in the analysis.

Fatigue crack growth is monitored using a dual cantilever clip-on displacement transducer – model UB-5 A from TML – mounted directly on the integral knife edges at the crack mouth. The fatigue crack growth, $\mathrm{d}a/\mathrm{d}n$, is presented as a function of ΔK at a double logarithmic scale. The $\mathrm{d}a/\mathrm{d}n$ is the average over a fixed ΔK-step size. Table 3 presents the cyclic loading conditions.

The plane-strain fracture toughness is the material property that describes the critical condition for the onset of unstable crack growth under plane-strain. It is expressed as the critical stress intensity factor, K_{IC}. The scalar K_I represents the stress field close to the tip of a crack [31], and is calculated as:

$$K_I = \alpha\sigma(\pi a)^{1/2}, \tag{1}$$

Table 3
Loading conditions of the specimens in the fatigue crack growth tests.

Specimen	P_{max} [kN]	Load ratio, R
1	4.0	0.1
2	4.0	0.5
3	3.5	0.1
4	6.0	0.5

with α being the geometrical factor for test specimens of finite size provided in ASTM E399 [18], σ the stress in the nominal cross section (without considering the presence of the crack) and a the crack length.

To determine the fracture toughness first a fatigue pre-crack was induced in the specimens by applying constant amplitude loading characterized by a load ratio $R < 0.1$ and a maximum force $P_{max} \leq 10\,\text{kN}$, as presented in Table 5, Section 3. During pre-cracking, the crack size was monitored using compliance measurement based on crack mouth opening displacement, v. The compliance, u, is calculated as [17]:

$$u = \left[\left(\frac{EvB}{P}\right)^{1/2} + 1\right]^{-1}, \tag{2}$$

where E is the Young's Modulus and P the applied load. To minimize the effect of crack closure on compliance reading, Eq. (2) is evaluated at 90% of the load, at the descending part of the constant amplitude loading cycle [32].

The normalized crack length is, for C(T)-specimens, calculated as [18]:

$$\frac{a}{W} = 1.0010 - 4.6695u + 18.460u^2 - 236.82u^3 + 1214.9u^4 - 2143.6u^5, \tag{3}$$

with a being the crack length and W the specimen width.

Secondly are the fracture toughness tests performed by applying an increasing load at a constant rate up to fracture, and such that the increase of the stress intensity factor is between 0.55 and 2.75 MPa $\text{m}^{1/2}/\text{s}$ for quasi-static testing in accordance with ASTM-E399 [18].

The load–displacement plot is analyzed following the procedure for determination of the fracture toughness, reported in Annex X of ASTM E399 [18]. In this procedure, the slope of the secant to the load–displacement curve, used to identify the load for fracture toughness determination, is dependent on the ligament and not fixed to 95%. This waives the condition for a test to be valid, that the maximum load should not be larger than 1.1 P_Q, which is defined as the load at pop-in or the intersection with the secant line, depending on the principal type of the load–displacement record [18]. The secant offset percentage, S_Q, is a function of the ligament of the crack, defined as W - a, and is related to a constant crack extension. The 95% offset secant is based on a crack extension that is a constant fraction of the final pre-crack size [33].

The same test setup and analysis procedure has been employed by Leonetti and Schotsman [23] and Leonetti et al. [24] to determine plane-strain fracture toughness and fatigue crack growth rate of the R350HT rail steel.

The length of the fatigue pre-crack in the fracture toughness specimens is the sum of the notch depth and the length of the fatigue crack emanating from that notch. The notch depth is measured on both sides of the fractured specimens using an Olympus Stereo SZX9 microscope, and averaged. The length of the fatigue crack is then measured using a Keyence VX5000 optical microscope. The measurement positions are provided by ASTM E399, i.e. at the intersection with the free surfaces, at 25%, 50%, and 75% of the thickness, resulting in a total of 5 measurements per specimen. The average of the measurements conducted at 25%, 50%, and 75% is used as the fatigue crack length [18].

2.3. Metallographic preparation and observations

The observations for fractographic analysis of the tensile, crack growth, and fracture toughness specimens are made after 30 min ultrasonic cleaning in isopropanol, using a Jeol IT100 Scanning Electron Microscope (SEM), with a 15 kV acceleration voltage and 10 mm working distance in secondary electron imaging mode.

Higher magnification micrographs of the microstructure were obtained with a Helios G4 PFIB UXe SEM using a 10 kV accelerating voltage, 0.1 nA current, and secondary electron imaging detection mode.

For the characterization of the tensile test specimens cross-section samples were made and embedded in conductive resin. Standard metallographic sample preparation was performed followed by chemical etching with Nital diluted to 2% for 10 s. Three lines of Vickers microhardness measurements were made at the specimen center and close to the free surface using a Durascan 70 hardness tester by applying a load of 10 N for 10 s. As a reference, 5 lines of hardness measurements were made on the rail head center of the unused rail. Successively, high-magnification images of the microstructure are made using a SEM model Jeol 6500F, with a working distance of 10 mm, and an acceleration voltage of 20 kV.

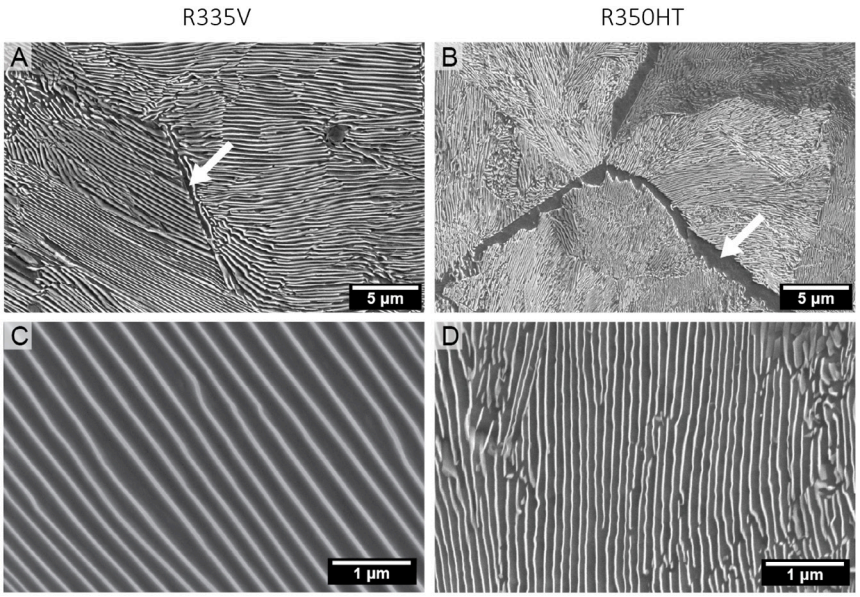

Fig. 2. Scanning electron micrographs of the as-received R335V [A, C] and R350HT [B, D] steels (respectively). [A, B] The pearlitic microstructure with white arrows indicating the presence of smaller and wider boundary ferrite networks. [C, D] The greater respectively smaller lamellar thickness, as is visually observed on the SEM images.

Table 4
Tensile test results of R335V, R350HT and Ref1 and Ref2.

Steel	E (GPa)	σ_y [MPa]	σ_{UTS} [MPa]	ϵ(%)	n
R335V [7]	210 ± 5	700 ± 11	1161 ± 12	8.2 ± 0.2	0.253 ± 0.003
R350HT [23]	219 ± 6	839 ± 8	1232 ± 8	10.4 ± 0.5	0.196 ± 0.002
Ref1 [9]		731	951	15.5	
Ref2 [25]		533	924	12	0.249

3. Results

3.1. Microstructure

Fig. 2A presents the micrograph of the as-received R335V steel grade evidencing the pearlitic microstructure and the presence of localized boundary ferrite. The presence of a ferrite layer has also been observed in other hypereutectoid steels [34,35] and is a result of silicon alloying and vanadium carbide formation [7,36]. However, coarse cementite particles are present at these boundaries. In a study on microstructural characterization of R335V Mattos Ferreira [7] observed the presence of randomly distributed VC-precipitates strengthening the cementite. Fig. 2B presents the microstructure of R350HT rail steel as a reference. A wider pro-eutectoid ferrite network is present.

High-magnification SEM images, Figs. 2C and D, qualitatively show the lamellar thickness. For R335V this is larger when compared to R350HT. The observations are made on a sectioning plane perpendicular to the lamellae.

Fig. 3 shows the hardness measured at the rail head center starting 0.5 mm from the surface. R335V rail steel has an average hardness of 351 ± 12 HV, while R350HT steel has an average hardness of 379 ± 9 HV. The hardness of standard grade Ref1, which has a similar carbon content as R350HT, is 288 ± 2 HV [9].

The absence of the continuous network suggests a larger volume fraction of cementite to be present in the pearlite [37]. Both the VC-precipitation and the increased cementite fraction contribute to hardness.

3.2. Results of the linear elastic fracture mechanics tests

3.2.1. Tensile behavior

Performing monotonic tensile tests is a pre-requisite to determine the settings of the LEFM-tests. Additionally, the interpretation of the shape of the stress–strain curve delivers valuable information about the response of the steel, whereas the fractography provides insight into the crack path and the microstructure relationship.

Table 4 shows the tensile test results with the standard deviation of the average for the tests on R335V [7] and R350HT [23]. In the same table are the results for standard grades Ref1 [9] and Ref2 [25] presented. The ultimate tensile stress, σ_{UTS} [MPa],

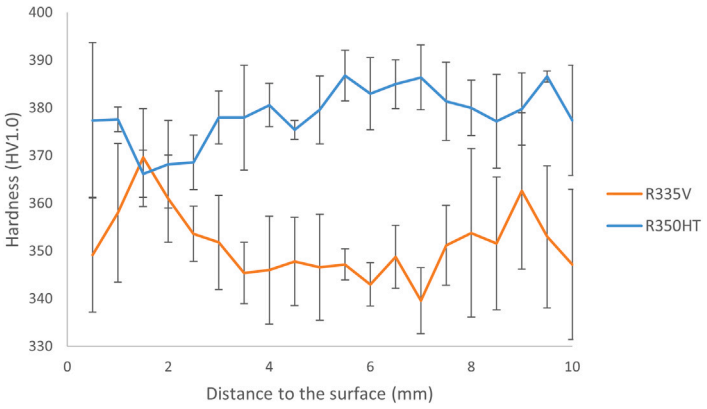

Fig. 3. Hardness of R335V and R350HT, measured on a transverse section of the rail head, at the centerline of the rail profile.

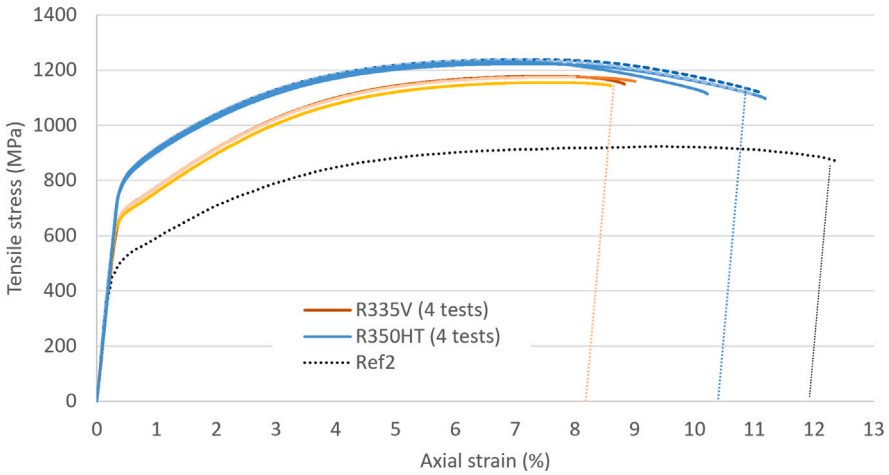

Fig. 4. Engineering stress–strain curves of the four tests of R335V [7]. The four test curves of R350HT [23] and Ref2 [25] are presented as a reference.

is defined as the maximum load, [N], divided by the undeformed area of the specimens, [m^2], σ_y [MPa] as the 0.2%-offset yield strength, and ϵ as the plastic elongation at fracture, measured over the parallel length of the specimens.

The strain hardening capacity of the steels is presented as the strain hardening exponent n, the exponent of the true stress as a function of true strain for the uniform plastic deformation, which is used to compare the strain hardenability of steels [38]. The results for R335V and R350HT are calculated from the available tensile test results [7,23]. For Ref2 n is presented in the literature [39].

Fig. 4 presents the monotonic stress–strain curves that were obtained for R335V, in orange, in blue the R350HT results, and in black results for standard grade Ref2 [25]. The lines parallel to the elastic part of the curve indicate the average total plastic elongation at fracture. Two additional aspects of the material response to the increasing tensile stress are considered. First the strain during elastic–plastic transition, an indication how the material starts yielding, and secondly the non-uniform material deformation, after necking.

For R335V the yielding evolution is sudden and limited necking takes place as such a very limited stress reduction is observed. Table 4 shows a gradual transition from elastic to plastic elongation in the tensile curves of R350HT steel. After reaching σ_{UTS} non-uniform deformation sets in, until fracture, at a, compared to R335V, larger plastic strain. Also Ref2 steel shows a gradual transition to plasticity and even more plastic strain at fracture.

3.2.2. Deformation and fractography of tensile specimens

Fig. 5 presents the microstructural observations on the transverse plane of the tensile specimens. Limited non-uniform deformation is observed in R335V which is also evidenced by the parallel specimen sides and small shear lips in Fig. 5A. Secondary cracks cut through the ferrite between the cementite lamellae and the crack tip blunting within the pearlite colony is an indication of local yielding, Fig. 5B. The coloration of the specimen is the result of maintaining the specimen at 200 °C, Fig. 5C [40].

In R350HT steel, Fig. 5D, the deformation results in necking and large shear lips. The secondary cracks are predominantly observed in the grain boundary ferrite, Fig. 5E.

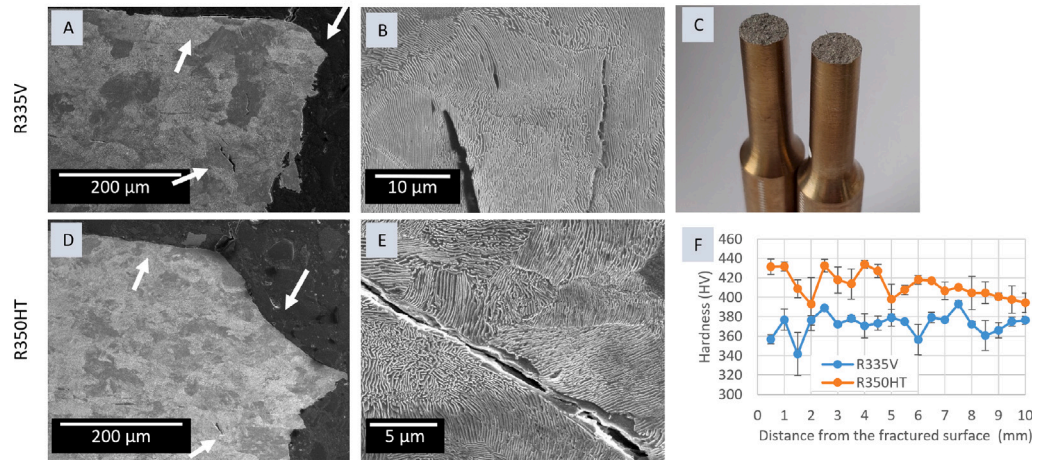

Fig. 5. Deformation observed in the transverse plane of the tensile specimens. (A) Cross-section of R335V tensile specimen. The arrows point the small shear lip and secondary cracks. (B) Secondary cracking in R335V. (C) The fractured R335V-specimens. (D) Cross-section of R350HT. The arrows indicate the shear-lip size and secondary cracking. (E) Secondary crack in R350HT. (F) Hardness measurement results on the cross-section.

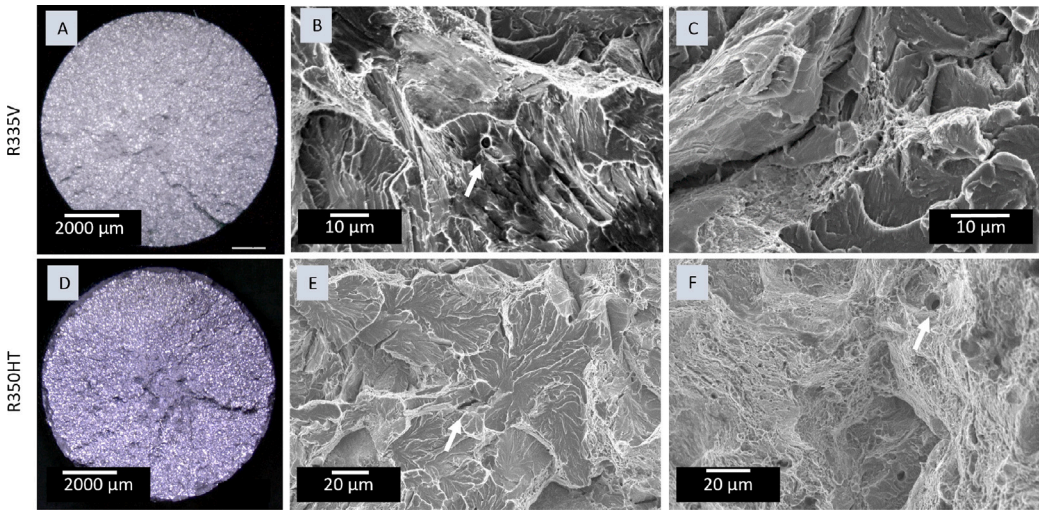

Fig. 6. Fractography of R335V (A–C) and R350HT (D–F) tensile specimen. The arrows indicate inclusion sites in areas showing cleavage and ductile fracture.

The strain-hardening properties of the steel and non-uniform deformation during the tensile tests result in the hardness trend over the cross-section as presented in Fig. 5F. In R335V the hardness is virtually independent of the distance to the fracture surface, whereas the measured hardness in the R350HT tensile specimen is high close to the fractured surface and decreases gradually with increasing distance.

Fig. 6 shows the fractographic images of the tensile specimens. In Fig. 6A is the presence of a circular wavy pattern of ridges at the R335V surface shown. Fig. 6B and C show SEM images of representative locations on the central part of the fractured surface. The presence of clean cleavage-fracture facets is shown in Fig. 6B. In the center of the micrograph a grain boundary is observed that encloses an area of brittle rupture. Only very limited ductile tearing patches are present and dimples are shallow, Fig. 6C.

In R350HT a limited number of ridges are present and at the outer region a small cup-and-cone fracture is observed, Fig. 6D. At the fracture surface, cleavage fracture areas are interspersed with areas showing ductile fracture features. The arrow in Fig. 6E points at an inclusion site, typically present at the center of the cleavage plane. At several positions patches with equiaxed dimples are observed. The arrow in Fig. 6F points at a larger inclusion site in the ductile fracture zone.

3.2.3. *Plane-strain fracture toughness*

The fracture toughness test results of R335V steel are presented in Table 5. Columns $P_{max,p}$, the maximum force during the pre-crack procedure, and a, crack length, contain the test information concerning the propagation of the fatigue pre-crack. To limit the influence of the crack-tip plastic zone on the fracture toughness results, the maximum force during the final stage of the pre-cracking

Table 5
Linear elastic plane-strain fracture toughness test results.

	Specimen	Precracking		Fracture toughness test			
		$P_{max,p}$ [kN]	a [mm]	P_{Qsi} [kN]	P_{max} [kN]	K_Q [MPa m$^{0.5}$]	K_{Isi} [MPa m$^{0.5}$]
R335V	1	10	18.9	14.8	16.1	36.7	*
	2	10	18.7	13.4	16.5	32.7	*
	3	9.0	19.2	13.7	15.7	34.7	*
	4	9.0	18.9	12.6	15.7	31.1	*
	5	8.0	20.1	14.8	17.6	36.1	36.1
	6	8.0	20.4	14.4	17.3	35.9	35.9
	7	8.0	20.2	14.0	18.2	37.5	37.5
						34.9 ± 0.9	36.5 ± 0.5
R350HT [23,24]	1	11.0	21.1	14.4	16.8	37.8	*
	2	10.5	20.5	15.6	20.0	39.0	*
	3	9.45	19.1	14.9	16.9	33.7	33.7
	4	10.5	18.7	15.5	18.0	34.0	*
	5	10.5	18.8	15.9	19.2	35.3	*
	6	8.6	19.3	17.1	20.6	39.1	39.1
	7	8.6	20.2	15.8	18.7	38.6	38.6
	8	8.6	20.0	15.4	19.3	37.1	37.1
						36.8 ± 0.8	37.1 ± 1.2
Ref1 (L-S) [9]							38.6
Ref2 [25]							32.5 ± 2.3

* Invalid: $P_{max,p} > 0.6P_{Qsi}$.

is limited to $P_{max,p} > 0.6P_{Qsi}$. Also, the fatigue pre-crack length is limited to $0.45 \leq a/W \leq 0.55$, with a/W the ratio of crack length and specimen width [18].

The last four columns contain the test results. P_{Qsi} is the intersect of the force–displacement-curve with the secant line. P_{max}, the maximum force in the force–displacement-curve, and K_Q the conditional result. If the K_I-test satisfies the conditions for plane-strain, K_Q can be considered K_{ISi}. In Table 5 the invalid results are indicated with an asterisk.

The test results of R350HT are shown as well [23,24]. At the bottom rows the fracture toughness of Ref1, tested on samples having the same orientation [9] and Ref2 [25] are presented. To summarize the results, statistically no difference between the K_{Isi} of R335V and R350HT is observed.

3.2.4. Fractography of the fracture toughness specimens

Fig. 7 shows the fracture surface of R335V fracture toughness specimens with in Fig. 7A the specimen with knife-edge and straight notch. Details of the surface, typical for R335V, are presented in Figs. 7B–F. The frames in Fig. 7A present the indicative observation locations.

The cleavage planes in Fig. 7B are observed at a crack length $a = 32$ mm. It is shown that from each cleavage plane a successive cleavage fracture initiates. The crack front then waves out within the plane, in the direction indicated by the river lines. Outside that area it is observed that several cleavage planes have a ~90° angle. This angle is associated with the ferrite cubic BCC crystal structure [9]. The cleavage tends to advance along the (100)-plane [10].

Ductile patches are present but only small, ranging from 20 μm to 50 μm in size. A detail of the ductile fracture characteristics is presented in Fig. 7C. The typical hole-joining features, like dimples, are superficial, not fully developed, even at this relatively large crack length. This might be caused by the thin and localized grain-boundary ferrite present in the microstructure. The shallow, vein-like patterns, and 'fluted' river lines are also associated with ductile separation [31,41].

In Fig. 7D a detail in the framed area in Fig. 7B is shown. The coalescence of crack planes results in the river lines at the cleavage fracture plane [31]. The resulting step sizes vary in height and orientation.

In Fig. 7E the transition zone between the fatigue pre-crack and cleavage fracture is presented. At the right the fatigue pre-crack with a fatigue-related staircase surface pattern is observed, with a sudden transition to the brittle cleavage fracture at the left. The arrows at the surface indicate the local propagation direction. In between both areas a local stretch zone is present. The stretch zone is a zone of plastic deformation and fibrous hole-joining fractures that occur at the tip of the fatigue crack before unstable growth by cleavage [31]. This is locally observed and shown in Fig. 7F.

To summarize the observations for R335V, the cleavage planes initiate and re-initiate, and ductile patches are small. Tear ridges at a ~90° angle are present, evidencing the cleavage plane propagation in the (100)-planes as predicted by Park and Bernstein [10] following a path through the effective grain, a concept that describes the composed unit of pearlitic colonies with low mutual misorientation.

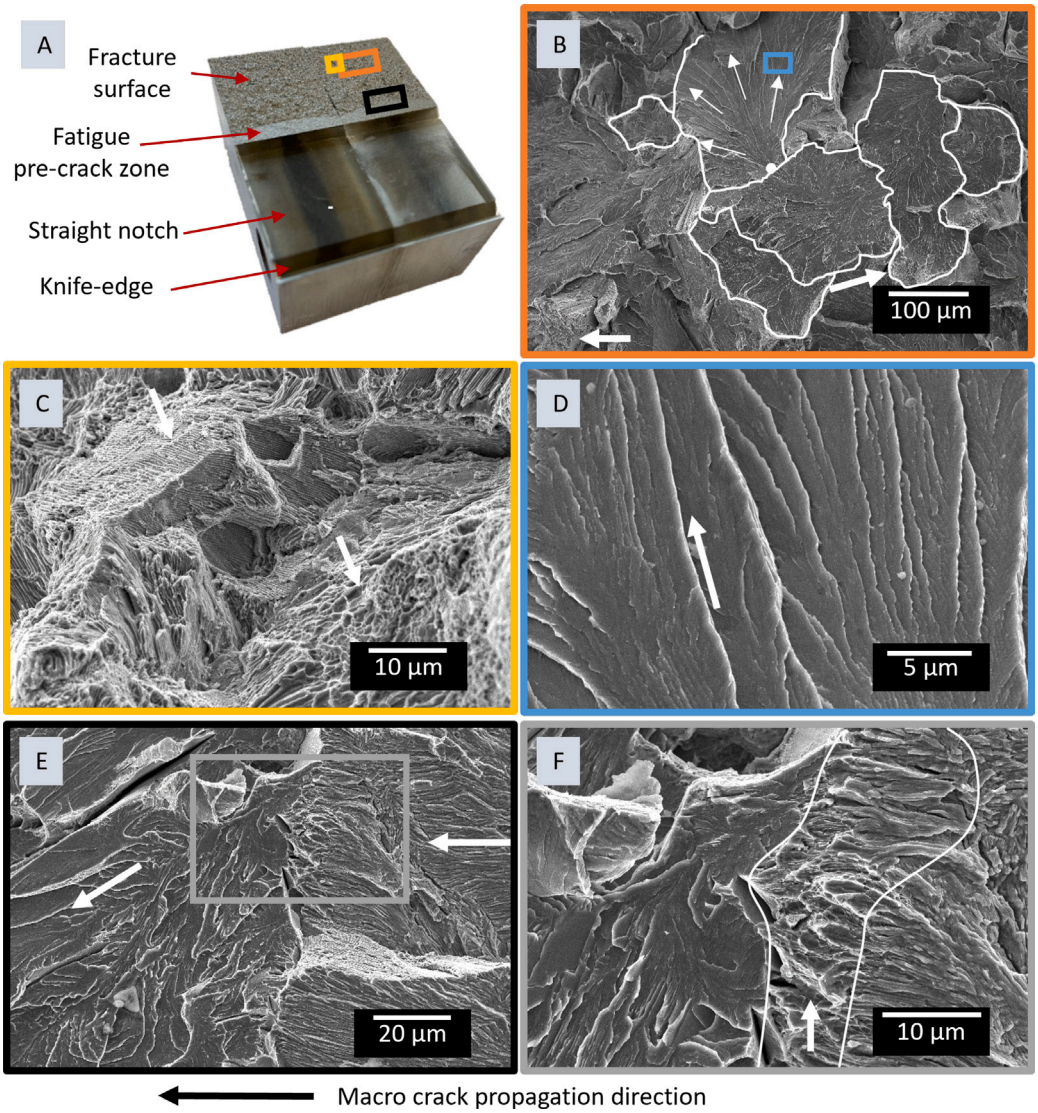

Fig. 7. Fractographic micrographs of R335V fracture toughness specimen. [A] The fractured specimen with observation locations. [B] The cleavage fracture zone with low mutual misorientation angle colonies. The re-initiation site with local propagation direction is indicated. [C] An area with ductile fracture; the lamellar structure with fluted ductile fracture characteristics. [D] River patterns in the cleavage fracture zone. [E] The transition zone from fatigue pre-crack to cleavage fracture. [F] Stretch zone.

Table 6
Paris–Erdogan crack growth parameters for R335V, R350HT, and referenced steel grades, for load ratios $R = 0.1$ and $R = 0.5$.

	$R = 0.1$		$R = 0.5$	
	C (m/cycle) /(MPa$\sqrt{\text{m}}$)^m	m	C (m/cycle) /(MPa$\sqrt{\text{m}}$)^m	m
R335V	3.47×10^{-13}	4.20	7.64×10^{-13}	4.31
R350HT [23]	4.11×10^{-13}	3.92	4.90×10^{-13}	4.09
Ref1 (L-S) [9]	2.30×10^{-13}	3.98		
Ref2 [39]	5.95×10^{-13}	3.86	1.14×10^{-12}	3.96

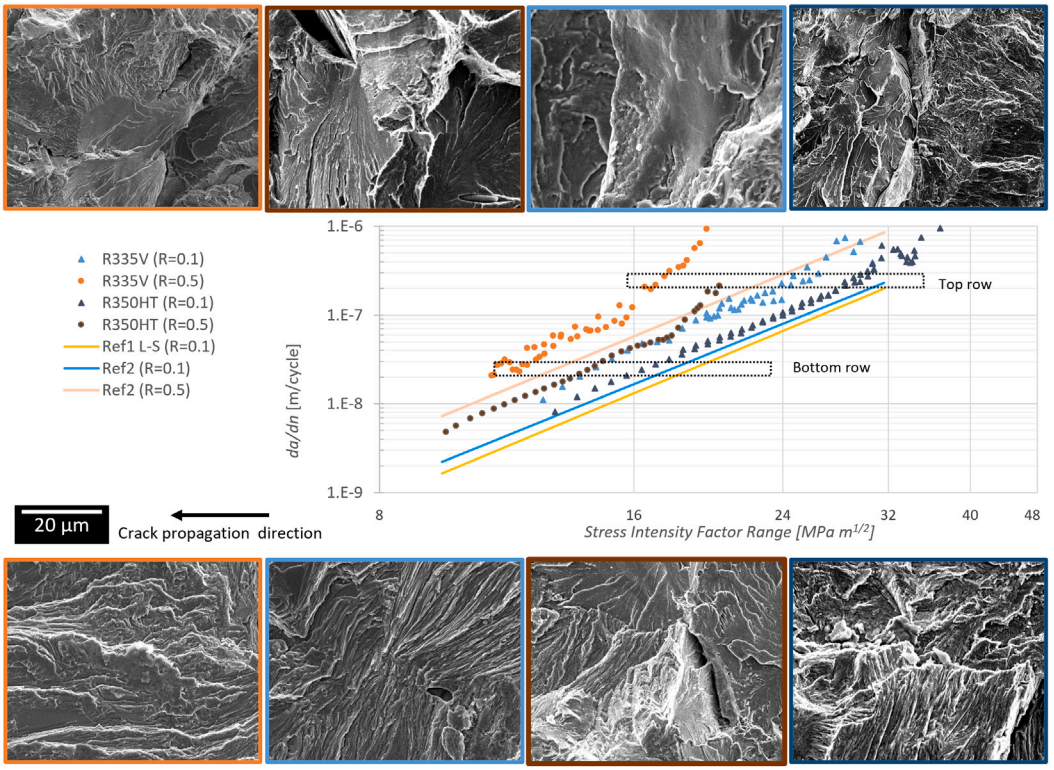

Fig. 8. Fatigue crack growth graphs. The results for R335V and R350HT [23] are presented together with Paris-curves from Ref1 [9] and Ref2 [25]. Fractographic images at equal crack growth; top row $da/dn \sim 2.5 \times 10^{-7}$ m/cycle, bottom row $da/dn \sim 2.5 \times 10^{-8}$ m/cycle. The image frame colors correspond with the graph colors.

3.2.5. Fatigue crack growth

In this study the crack growth of R335V steel is tested in a wide ΔK range and subsequently analyzed in the Paris-regime, as described by the Paris–Erdogan law:

$$\frac{da}{dn} = C\Delta K^m, \tag{4}$$

with da/dn the crack growth rate in [m/cycle], ΔK the stress-intensity factor range [MPa$\sqrt{\text{m}}$], and C [(m/cycle) /(MPa $\sqrt{\text{m}}$)^m] and m material parameters.

Table 6 presents the Paris–Erdogan material parameters for stress ratios $R = 0.1$ and $R = 0.5$, and also the test results for R350HT rail steel [23] and Ref2 [25], both using C(T)-specimens, and Ref1 steel [9] using SE(B) specimens.

The fatigue crack growth rate curves for R335V rail steel are presented in Fig. 8, in blue for the load ratio $R = 0.1$, and for $R = 0.5$ in orange. Fig. 8 further shows the fatigue crack growth curves for R350HT [23] and the Paris curves for Ref1 [9] and Ref2 [39].

Fracture surfaces of equal crack growth rates are presented for R335V and R350HT. All pictures are at the same magnification as is represented by the single scale bar, and the colored frames correspond with the graph colors.

The R335V graph for $R = 0.1$ is linear at the lower stress intensity factor range, in this double-log graph. Scatter in the results increases from $\Delta K \sim 24$ MPa m$^{1/2}$. For stress ratio $R = 0.5$ it is observed that the crack growth accelerates, entering stage III crack growth at $\Delta K \sim 17$ MPa m$^{1/2}$.

In the fractographic images a staircase pattern, associated with fatigue crack growth, is observed at a stress ratio of $R = 0.1$ and $\sim da/dn = 2.5 \times 10^{-8}$ m/cycle. The surface is almost flat. At $R = 0.5$, tear ridges are present and parallel cleavage planes are observed. Then, at the top row the crack growth is a factor 10 higher. At $R = 0.1$, still in stage II fatigue crack growth, cleavage planes with river lines are observed next to areas showing fatigue crack growth. The fracture surface of R335V tested at $R = 0.5$ is characterized by the cleavage planes at a high mutual angle. At the verge of these planes, crack arrest and re-initiation in fatigue crack growth takes place.

The fatigue crack growth graphs for R350HT show similar characteristics as for R335V, although the crack growth rate is lower at the same stress intensity factor range. For $R = 0.1$, the graph is linear at low ΔK, and scatter increases at $\Delta K \sim 32$ MPa m$^{1/2}$. For stress ratio $R = 0.5$ the graph is linear at the lower ΔK range, and the crack growth rate accelerates, entering stage III crack growth at $\Delta K \sim 18$ MPa m$^{1/2}$.

The fractographic images of R350HT show a fine staircase pattern, which is associated with the small lamellar thickness, at $R = 0.1$ and $da/dn \sim 2.5 \times 10^{-8}$ m/cycle. Increasing the stress ratio to $R = 0.5$ reveals several features such as cleavage planes, and crack arrest and re-initiation.

At the top row, at $R = 0.1$, small cleavage planes are observed showing high mutual angles, and in the micrograph, also signs of crack arrest and re-initiation are observed. The fracture surface of R350HT tested at $R = 0.5$ has different characteristics. Next to brittle cleavage facets, tear ridges are present at which ductile hole-joining features are observed.

Fig. 9 presents the fracture surface characteristics for the fatigue crack growth in R335V tested at $R = 0.1$. The crack length is derived from the calibrated gauge opening displacement. Fig. 9A shows a 5 μm wide stretch zone between the straight crack starter notch in the specimen and a brittle cleavage crack start. In Fig. 9B local growth directions are indicated with the arrows. The crack growth path follows microstructural features, like grain boundaries and ferrite laths, despite being in the Paris-regime [13,15]. The observed changes in orientation might be related to a grain boundary, seen as the ridge in the Figure. The small cleavage zone in the further fatigue growth-dominated surface in Fig. 9C is interpreted as a step or bifurcation in the crack path. When the crack length increases, in Fig. 9D, quasi-cleavage zones with crack arrest and re-initiation zones are observed. Upon further growth, fatigue crack growth and parallel cleavage planes are present at close distance, see Fig. 9E. Fig. 9F shows the surface close to the onset of unstable crack propagation. Cleavage planes increase both in density and size. Tear ridges between the planes are present, and some fatigue crack growth zones are still observed.

To summarize the observations regarding crack growth in R335V steel. At low fatigue crack growth rates the crack path clearly follows microstructural features. Fractography shows that fatigue crack growth characteristics are locally present even close to unstable fracture.

4. Discussion

The tensile behavior, plane-strain fracture toughness and fatigue crack growth rate results are discussed with respect to the microstructure characteristics of R335V and compared to the results of R350HT [23].

4.1. Tensile behavior

The steel composition and production route of R335V result in a specific tensile behavior for rail steel grades when compared to other grades mentioned in the prEN13674-1 [26],

The strain hardening coefficient of R335V is high. In Table 4 is the coefficient, $n = 0.253 \pm 0.003$, presented, together with values for the referenced steels [23,39]. This value is higher compared to R350HT [23] and also higher than that of standard grade Ref2 steel [39]. As a result, σ_{UTS} of R335V is only 6% lower than of R350HT whereas the 0.2%-offset yield strength is 17% lower.

Strain hardening is largely controlled by dislocation motion in the pearlitic ferrite, and it therefore increases with the lamellar thickness [3,42,43]. Measurement of the lamellar thickness is often performed in studies on the structure–property relation [44]. The difference in lamellar distance between the R335V and the R350HT rail steel can be observed by comparing Figs. 2C and D, together with the presence of a small and wide (respectively) boundary ferrite network as shown in Figs. 2A and B. The air-cooling after hot rolling of the R335V has resulted in a relatively larger lamellar thickness whereas accelerated cooling of R350HT resulted in the smaller lamellar thickness.

Hardness on the other hand, holds a Hall–Petch relation with the lamellar thickness [10,16,45]. The average hardness of R350HT, as measured at the centerline of the rail profile, is 379 ± 9 HV, which is higher than for the air-cooled standard grade Ref1. Ref1 has a similar carbon content and a hardness of 288 ± 2 HV [9]. The R335V rail steel has an overall hardness of 351 ± 12 HV. The VC-precipitation is known to prevent the formation of a continuous proeutectoid cementite network [7,21,46], resulting, with silicon addition, in a higher cementite-ferrite ratio within the pearlite and higher hardness than can be expected from the lamellar thickness itself [37].

4.2. Plane-strain fracture toughness

Table 5 presents the results of the plane-strain fracture toughness tests. Fracture toughness tests are often part of material acceptance, in which minimum requirements on K_{IC} are defined. Despite the hypereutectoid composition of R335V, statistically no difference in fracture toughness between R335V and R350HT [23] is observed. These results are in line with results in other studies on rail steels [9,11,47].

Differences in the fracture toughness values of pearlitic rail steels are explained in the literature by two different microstructural features, the lamellar thickness [4,11,12] and the effective grain size, the size of clusters of pearlite colonies with small mutual misorientation [9,10]. In deviation from the R335V steel, all rail steel grades in the referenced literature have a close to eutectoid composition [9,11,47], while the hyper-eutectoid composition is usually associated with lower fracture toughness [48].

Kavishe and Baker [4] conclude that higher lamellar thickness results in higher fracture toughness. This lamellar thickness-fracture toughness relation is not observed and therefore lamellar thickness is not the explaining factor in this experimental investigation. Fig. 7 presents the fractured surface of a R335V specimen, and in the detailed Fig. 7B the area of parallel cleavage planes is encircled. In agreement with Park and Bernstein [10], the crack re-initiates at adjacent colonies when cleavage propagates. In steels with low mutual misorientation between colonies, little energy is consumed for this re-initiation, and as a result fracture toughness is low. Therefore, the fracture toughness of the steel is explained by the effective grain size.

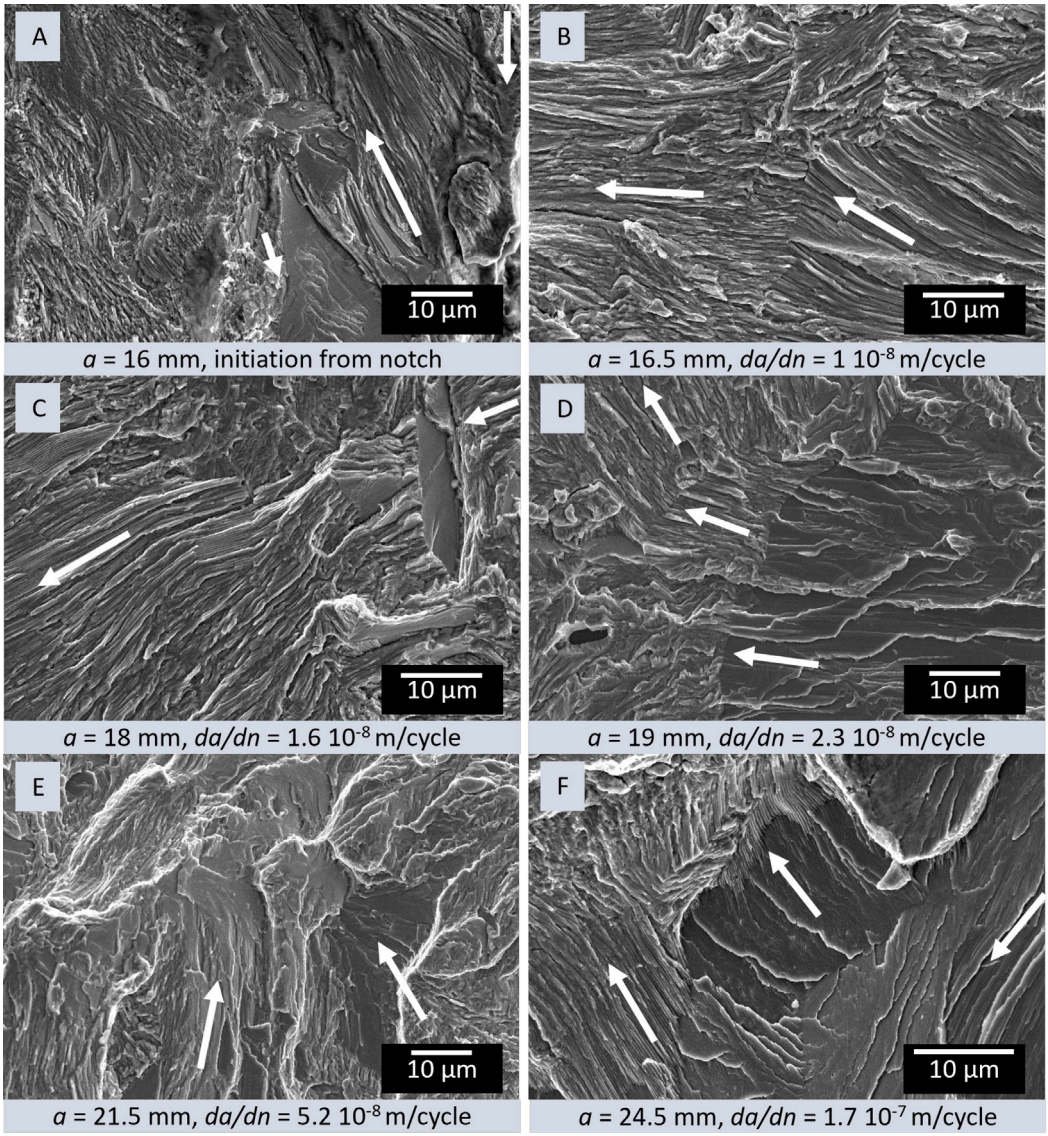

Fig. 9. Fractography of fatigue crack growth of R335V, tested at R = 0.1. The images are ordered by crack length. The crack length and crack growth rate are indicated under each image. The white arrows indicate local crack propagation direction, whereas the macro crack growth is from right to left. [A] Crack initiation at the straight notch. [B] Fatigue crack propagation with microstructure-related transition. [C] Fatigue crack propagation with local cleavage zones. [D] Crack arrest and re-initiation. [E] Area fraction of cleavage zones increases. [F] Quasi-cleavage crack propagation and fatigue crack propagation.

To explain the similar fracture toughness values for R335V and R350HT, despite the differences in composition and lamellar thickness, is the production route of both rails observed. Reheating of the blooms and the consecutive hot rolling of the rails, and recrystallization after each rolling step, is the standard procedure for the production of the rails from both steel grades. The present study indicates that this production route results in similar sized effective grains, regardless of the cooling rate after hot rolling.

4.3. Fatigue crack growth

In Table 6 and Fig. 8 are the fatigue crack growth rate test results presented. The fatigue crack growth in both R335V and R350HT [23] rail steels are determined using the same test setup, and similar sized C(T)-specimens.

Increasing the stress ratio increases the mean stress intensity factor, limits crack closure phenomena, and results in higher crack growth rate in R335V, R350HT [23] and Ref2 [25], as is observed in Fig. 8. This is a well-known effect [9,47,49].

The fatigue crack growth curves in Table 6 are parallel, although for R335V higher fatigue crack growth rates are observed. A small lamellar thickness is associated with a more ductile fracture behavior, with more secondary cracking [15], and with the best resistance to crack growth at low crack growth rates [13]. For small-scale yielding conditions this is explained by the radius of the

plastic zone, r_y, which can be estimated as the squared ratio of the actual value of K_1 and the yield strength of the material [50], according to

$$r_y \approx \frac{1}{2\pi}\left(\frac{K_1}{\sigma_y}\right)^2. \tag{5}$$

A smaller lamellar thickness results in a higher resistance to yielding and retards crack growth [13].

Moreover, the composition of R335V steel is hypereutectoid with 0.91 wt% carbon content, as is presented in Table 1, whereas Daeubler et al. [15] used AISI1080 in their experimental investigation, with a carbon content of 0.8 wt%. Mishra et al. [13] used steel with a carbon content of 0.72 wt%. Therefore, besides lamellar thickness, a second aspect is discussed; the cementite network at the prior austenite grain boundary.

The composition of R335V is optimized with manganese, silicon and vanadium additions [5,36,51]. The manganese addition limits prior-austenite grain size, contributing to the toughness [8], whereas the silicon prevents the formation of pro-eutectoid cementite [36]. Mattos Ferreira [7] observed the presence of a limited layer of grain boundary ferrite in the microstructure of R335V, in which also coarse cementite particles are present, this microstructure has been illustrated in Fig. 2A.

A limited number of studies is available to reference fatigue crack growth in pearlitic hypereutectoid steels. However, despite the attention to the cementite network at the prior austenite grain boundary, Thao [37] concluded that the fatigue crack growth rate in hypereutectoid steels is higher than in eutectoid steels. This is explained by the brittle fracture through the grain boundaries or the lower deformation capacity of the microstructure having a higher cementite content [37].

5. Conclusions

In this experimental investigation, the mechanical behavior of an air-cooled vanadium-alloyed hypereutectoid rail steel is characterized using standardized linear elastic fracture mechanics tests. The main conclusions are summarized below:

- The monotonic tensile test results have shown that the strain hardening capacity of R335V steel is higher than that of R350HT rail steel, a material property that is typically related to coarser pearlite. In the hypereutectoid steel non-uniform plastic elongation before fracture is virtually absent. The secondary cracks in R335V are at the ferrite-cementite interphase within the colony. Crack tip blunting is observed at the extremes of the secondary interphase cracks.
- The fractography of the tensile specimens show the clear grain boundaries in the fracture region. Ductile fracture patches are present but small as a result of the thin grain boundary ferrite. Additionally, at the fracture surface of the R335V fracture toughness specimens, it is observed that ductile fracture features like dimples are shallow.
- Statistically is no difference between the fracture toughness of R335V and R350HT rail steel observed. The fracture toughness tests are performed at room temperature. This result indicates that a damage-tolerant maintenance strategy of the railway rails can be applied when R335V steel rails are installed.
- The fatigue crack growth curve in the Paris-regime of the mode-I fatigue crack growth test is parallel to the Paris curves of R350HT and standard grade eutectoid rail steels. Although being parallel is the fatigue crack growth resistance in the Paris regime lower for R335V. Despite the limited references available is the lower crack growth resistance explained by the hypereutectoid composition, and is, in the Paris regime, independent of the microstructure as optimized by the silicon, manganese and vanadium additions.
- The fractography of the fatigue crack growth surfaces shows a coarse staircase pattern. At high ΔK it is observed that the cleavage facets cover a larger area fraction, but still fatigue crack growth is observed. This heterogeneity is believed to contribute to the substantial scatter in the fatigue crack growth results.

The authors declare that they have no known competing financial interests or personal relationships that could have appeared to influence the work reported in this paper.

CRediT authorship contribution statement

B. Schotsman: Writing – review & editing, Writing – original draft, Visualization, Project administration, Methodology, Investigation, Formal analysis. **V. Mattos Ferreira:** Writing – review & editing, Writing – original draft. **D. Leonetti:** Methodology, Formal analysis, Conceptualization. **R.H. Petrov:** Writing – review & editing. **M.J. Santofimia:** Writing – review & editing, Visualization. **J. Sietsma:** Writing – review & editing.

Declaration of competing interest

The authors declare that they have no known competing financial interests or personal relationships that could have appeared to influence the work reported in this paper.

Acknowledgments

This research was carried out under project number S16042a and T18014 in the framework of the Partnership Program of the Materials innovation institute M2i (www.m2i.nl) and the Technology Foundation TTW, which is part of the Netherlands Organization for Scientific Research (www.nwo.nl). We would like to thank the Structures Laboratory Eindhoven - TU/e for the use of equipment and support, ProRail for its financial support and British Steel and Voestalpine Railpro for providing rail sections for this research.

Data availability

Data will be made available on request.

References

[1] Andrade CESD, D'Agosto MDA. Energy use and carbon dioxide emissions assessment in the lifecycle of passenger rail systems: The case of the Rio de Janeiro Metro. J Clean Prod 2016;126:526–36. http://dx.doi.org/10.1016/j.jclepro.2016.03.094.
[2] Alexander DJ, Bernstein IM. Cleavage Fracture in Pearlitic Eutectoid Steel. Metall Trans A 1989;20A:2321–35. http://dx.doi.org/10.1007/BF02666667.
[3] Dollar M, Bernstein IM, Thompson AW. Influence of deformation substructure on flow and fracture of fully pearlitic steel. Acta Metall 1988;36(2):311–20. http://dx.doi.org/10.1016/0001-6160(88)90008-9.
[4] Kavishe FPL, Baker TJ. Effect of prior austenite grain size and pearlite interlamellar spacing on strength and fracture toughness of a eutectoid rail steel. Mater Sci Technol 1986;2(8):816–22. http://dx.doi.org/10.1179/mst.1986.2.8.816.
[5] Solano-Alvarez W, Fernandez Gonzalez L, Bhadeshia HK. The effect of vanadium alloying on the wear resistance of pearlitic rails. Wear 2019;436–437(August):203004. http://dx.doi.org/10.1016/j.wear.2019.203004.
[6] Wilby A, Corteen J, Lewis S, Lewis R, Fletcher D. Efficient laboratory test programme for characterising rail steel strain accumulation. In: 12th international conference on contact mechanics and wear of rail/wheel systems. 2022, p. 62–70.
[7] Mattos Ferreira V. Microstructural phenomena in pearlitic railway steels [Ph.D. thesis], Delft University of Technology; 2024, http://dx.doi.org/10.4233/uuid:facb282f-74a1-446d-bbc6-5ed294602ed2.
[8] Hyzak JM, Bernstein IM. The role of microstructure on the strength and toughness of fully pearlitic steels. Metall Trans A 1976;7(8):1217–24. http://dx.doi.org/10.1007/BF02656606.
[9] Maya-Johnson S, Ramirez AJ, Toro A. Fatigue crack growth rate of two pearlitic rail steels. Eng Fract Mech 2015;138:63–72. http://dx.doi.org/10.1016/j.engfracmech.2015.03.023.
[10] Park YJ, Bernstein IM. The process of crack initiation and grain size for cleavage fracture in eutectoid steel effective pearlitic. Metall Trans A 1979;10A:1653–64. http://dx.doi.org/10.1007/BF02811698.
[11] Moreira Luiza Pessoa, Viana Thiago Gomes, Godefroid Leonardo Barbosa, de Faria Geraldo Lúcio, Cândido Luiz Cláudio. Effect of some microstructural characteristics on the fracture toughness and fatigue crack growth resistance of five different pearlitic steels for railroad application. In: Proceedings of the 23rd ABCM international congress of mechanical engineering. ABCM Brazilian Society of Mechanical Sciences and Engineering; 2015, http://dx.doi.org/10.20906/cps/cob-2015-0895.
[12] Godefroid LB, Souza AT, Pinto MA. Fracture toughness, fatigue crack resistance and wear resistance of two railroad steels. J Mater Res Technol 2020;9(5):9588–97. http://dx.doi.org/10.1016/j.jmrt.2020.06.092.
[13] Mishra K, Khiratkar VN, Singh A. Improvement of sub-critical fatigue crack growth life by nano-structuring of pearlite. Int J Fatigue 2019;122(January):84–92. http://dx.doi.org/10.1016/j.ijfatigue.2019.01.005.
[14] Gray GT, Williams JC, Thompson AW. Roughness-induced crack closure: An explanation for microstructurally sensitive fatigue crack growth. Metall Trans A 1983;14:421–33. http://dx.doi.org/10.1007/BF02644220.
[15] Daeubler MA, Thompson AW, Bernstein IM. Influence of microstructure on fatigue behavior and surface fatigue crack growth of fully pearlitic steels. Metall Trans A 1990;21A:925–33. http://dx.doi.org/10.1007/BF02656577.
[16] Lewandowski JJ, Thompson AW. Microstructural effects on the cleavage fracture stress of fully pearlitic eutectoid steel. Metall Trans A 1986;17A:1769–86. http://dx.doi.org/10.1007/BF02817275.
[17] ASTM. E647-15 - standard test method for measurement of fatigue crack growth rates. American Society of Testing Materials; 2008.
[18] ASTM. E399-20a - standard test method for linear-elastic plane-strain fracture toughness of metallic materials. American Society of Testing Materials; 2020.
[19] Ellyin F. Fatigue damage, crack growth and life prediction. Springer Science & Business Media; 2012.
[20] Richard HA, Sander M. Fatigue crack growth, vol. 18. Springer; 2016.
[21] Han K, Mottishaw TD, Smith GD, Edmonds DV. Effects of vanadium addition on nucleation and growth of pearlite in high carbon steel. Mater Sci Technol (United Kingdom) 1994;10(11):955–63. http://dx.doi.org/10.1179/mst.1994.10.11.955.
[22] Zerbst U, Lundén R, Edel K-O, Smith RA. Introduction to the damage tolerance behaviour of railway rails–a review. Eng Fract Mech 2009;76(17):2563–601. http://dx.doi.org/10.1016/j.engfracmech.2009.09.003.
[23] Leonetti D, Schotsman B. Experimental investigation on the fatigue and fracture properties of a fine pearlitic rail steel. Frattura Integr Strutturale 2024;18(69):142–53. http://dx.doi.org/10.3221/IGF-ESIS.69.11, URL https://www.fracturae.com/index.php/fis/article/view/4836.
[24] Leonetti D, Ferreira VM, Schotsman B. Fracture behavior and mechanical characterization of R350HT rail steel. Procedia Struct Integr 2023;47:219–26. http://dx.doi.org/10.1016/j.prostr.2023.07.015.
[25] Christodoulou PI, Kermanidis AT, Haidemenopoulos GN. Fatigue and fracture behavior of pearlitic Grade 900A steel used in railway applications. Theor Appl Fract Mech 2016;83:51–9. http://dx.doi.org/10.1016/j.tafmec.2015.12.017.
[26] CEN. prEN13674-1 - railway applications - rail - part 1: vignole railway rails 46 kg/m and above. European Committee for Standardization; 2023.
[27] Fischer FD, Hinteregger E, Rammerstorfer FG. The influence of different geometrical and thermal boundary conditions and the phase transformation on the residual stress state in railroad rails after heat-treatment. In: International conference on residual stresses. Springer; 1989, p. 467–72.
[28] ISO. EN-ISO6892-1 - metallic materials - tensile testing - part 1: method of test at room temperature (Iso 6892-1:2019). International Organization for Standardization; 2019.
[29] Balit Y, Joly LR, Szmytka F, Durbecq S, Charkaluk E, Constantinescu A. Self-heating behavior during cyclic loadings of 316L stainless steel specimens manufactured or repaired by Directed Energy Deposition. Mater Sci Eng A 2020;786. http://dx.doi.org/10.1016/j.msea.2020.139476.
[30] Munier R, Doudard C, Calloch S, Weber B. Determination of high cycle fatigue properties of a wide range of steel sheet grades from self-heating measurements. Int J Fatigue 2014;63:46–61. http://dx.doi.org/10.1016/j.ijfatigue.2014.01.004.
[31] Hull D. Fractography: observing, measuring and interpreting fracture surface topography. Cambridge University Press; 1999.
[32] Fleck N. Compliance methods for measurement of crack length. Eng Mater Advis Serv Ltd Fatigue Crack Meas Tech Appl (UK) 1991;1991:69–93.
[33] Wells DN, James MA, Allen PA, Wallin KR. A review of the proposed kisi offset-secant method for size-insensitive linear-elastic fracture toughness evaluation. Mater Perform Charact 2018;7(2).
[34] Parsons D, Malis T, Boyd J. Microalloying and precipitation in cr-v rail steels. J Heat Treat 1984;3(3):213–9. http://dx.doi.org/10.1007/BF02833263.
[35] Solano-Alvarez W, Peet MJ, Pickering EJ, Jaiswal J, Bevan A, Bhadeshia HK. Synchrotron and neural network analysis of the influence of composition and heat treatment on the rolling contact fatigue of hypereutectoid pearlitic steels. Mater Sci Eng A 2017;707(July):259–69. http://dx.doi.org/10.1016/j.msea.2017.09.045.
[36] Han K, Edmonds DV, Smith GD. Optimization of mechanical properties of high-carbon pearlitic steels with Si and V additions. Metall Mater Trans A 2001;32(6):1313–24. http://dx.doi.org/10.1007/s11661-001-0222-7.

[37] Phuong Thao B. Microstructural factors influencing fatigue crack growth mechanism in low-carbon and high-carbon steels [Ph.D. thesis], Nagaoka: Graduate school of engineering; 2021.
[38] Hajizad O, Kumar A, Li Z, Petrov RH, Sietsma J, Dollevoet R. Influence of microstructure on mechanical properties of bainitic steels in railway applications. Metals 2019;9(7). http://dx.doi.org/10.3390/met9070778.
[39] Christodoulou P, Kermanidis A, Haidemenopoulos G. Fatigue and fracture behavior of pearlitic grade 900a steel used in railway applications. Theor Appl Fract Mech 2016;83:51–9.
[40] Barwell FT, Bowen ER, Bowen JP, Westcott VC. The use of temper colors in ferrography. Wear 1977;44(1):163–71. http://dx.doi.org/10.1016/0043-1648(77)90093-X, URL https://www.sciencedirect.com/science/article/pii/004316487790093X.
[41] Bertolo V, Jiang Q, Tiringer U, Walters CL, Sietsma J, Popovich V. Cleavage fracture micromechanisms in thick-section quenched and tempered S690 high-strength steels. J Mater Sci 2022;57(42):20033–55. http://dx.doi.org/10.1007/s10853-022-07841-1.
[42] Hu X, Van Houtte P, Liebeherr M, Walentek A, Seefeldt M, Vandekinderen H. Modeling work hardening of pearlitic steels by phenomenological and Taylor-type micromechanical models. Acta Mater 2006;54(4):1029–40. http://dx.doi.org/10.1016/j.actamat.2005.10.030, URL https://www.sciencedirect.com/science/article/pii/S1359645405006427.
[43] Langford G. Deformation of Pearlite. Metall Trans A 1977;8A:861–75. http://dx.doi.org/10.1007/BF02661567.
[44] Vander Voort GF, Roósz A. Measurement of the interlamellar spacing of pearlite. Metallography 1984;17(1):1–17. http://dx.doi.org/10.1016/0026-0800(84)90002-8, URL https://www.sciencedirect.com/science/article/pii/0026080084900028.
[45] Mishra K, Singh A. Effect of interlamellar spacing on fracture toughness of nano-structured pearlite. Mater Sci Eng A 2017;706:22–6. http://dx.doi.org/10.1016/j.msea.2017.08.115.
[46] Han K, Mottishaw TD, Smith GDW, Edmonds DV, Stacey AG. Effects of vanadium additions on microstructure and hardness of hypereutectoid pearlitic steels. Mater Sci Eng A 1995;190(1–2):207–14.
[47] Godefroid LB, Moreira LP, Vilela TC, Faria GL, Candido LC, Pinto ES. Effect of chemical composition and microstructure on the fatigue crack growth resistance of pearlitic steels for railroad application. Int J Fatigue 2019;120(2018):241–53. http://dx.doi.org/10.1016/j.ijfatigue.2018.10.016.
[48] Krauss G. Steels: processing, structure, and performance. Asm International; 2015.
[49] Masoudi Nejad R, Farhangdoost K, Shariati M. Microstructural analysis and fatigue fracture behavior of rail steel. Mech Adv Mater Struct 2020;27(2):152–64. http://dx.doi.org/10.1080/15376494.2018.1472339.
[50] Suresh S, Ritchie RO. Propagation of short fatigue cracks. Int Met Rev 1984;29(6):445–75. http://dx.doi.org/10.1179/imtr.1984.29.1.445.
[51] Parsons SA, Edmonds DV. Microstructure and mechanical properties of medium-carbon ferrite–pearlite steel microalloyed with vanadium. Mater Sci Technol 1987;3(11):894–904. http://dx.doi.org/10.1179/mst.1987.3.11.894.